



## Article

# Shallow Sea Topography Detection from Multi-Source SAR Satellites: A Case Study of Dazhou Island in China

Longyu Huang <sup>1,2</sup>, Junmin Meng <sup>3,4,\*</sup>, Chenqing Fan <sup>3,4</sup>, Jie Zhang <sup>3,4</sup> and Jingsong Yang <sup>1,2,5,\*</sup><sup>1</sup> Ocean College, Zhejiang University, Zhoushan 316021, China<sup>2</sup> State Key Laboratory of Satellite Ocean Environment Dynamics, Second Institute of Oceanography, Ministry of Natural Resources, Hangzhou 310012, China<sup>3</sup> Laboratory of Marine Physics and Remote Sensing, First Institute of Oceanography, Ministry of Natural Resources, Qingdao 266061, China<sup>4</sup> Ocean Telemetry Technology Innovation Center, Ministry of Natural Resources, Qingdao 266061, China<sup>5</sup> Southern Marine Science and Engineering Guangdong Laboratory (Zhuhai), Zhuhai 519082, China

\* Correspondence: mengjm@fio.org.cn (J.M.); jsyang@sio.org.cn (J.Y.)

**Abstract:** Accurate measurement of underwater topography in the coastal zone is essential for human marine activities, and the synthetic aperture radar (SAR) presents a completely new solution. However, underwater topography detection using a single SAR image is vulnerable to the interference of sea state and sensor noise, which reduces the detection accuracy. A new underwater topography detection method based on multi-source SAR (MSSTD) was proposed in this study to improve the detection precision. GF-3, Sentinel-1, ALOS PALSAR, and ENVISAT ASAR data were used to verify the sea area of Dazhou Island. The detection result was in good agreement with the chart data (MAE of 2.9 m and correlation coefficient of 0.93), and the detection accuracy was improved over that of a single SAR image. GF-3 image with 3 m spatial resolution performed best in bathymetry among the four SAR images. Additionally, the resolution of the SAR image had greater influence on bathymetry compared with polarization and radar band. The ability of MSSTD has been proved in our work. Collaborative multi-source satellite observation is a feasible and effective scheme in marine research, but its application potential in underwater topography detection still requires further exploration.

**Keywords:** shallow sea topography; multi-source SAR; the linear dispersion relation; satellite bathymetry



**Citation:** Huang, L.; Meng, J.; Fan, C.; Zhang, J.; Yang, J. Shallow Sea Topography Detection from Multi-Source SAR Satellites: A Case Study of Dazhou Island in China. *Remote Sens.* **2022**, *14*, 5184. <https://doi.org/10.3390/rs14205184>

Academic Editor: Natascha Oppelt

Received: 29 August 2022

Accepted: 9 October 2022

Published: 17 October 2022

**Publisher's Note:** MDPI stays neutral with regard to jurisdictional claims in published maps and institutional affiliations.



**Copyright:** © 2022 by the authors. Licensee MDPI, Basel, Switzerland. This article is an open access article distributed under the terms and conditions of the Creative Commons Attribution (CC BY) license (<https://creativecommons.org/licenses/by/4.0/>).

## 1. Introduction

As a basic element of the marine environment, shallow sea topography is an essential parameter in marine economic construction, military activities, and marine scientific research. The coastal zone is the most frequent area of human marine activity, and accurate measurement of underwater topography is critical for coastal zone construction and ecological protection. Remote sensing can work continuously, and in large areas, it can observe the ocean surface with the advantages of high timeliness and high economy compared with the traditional multi-beam measurement by ships, which provides a new solution for the detection of underwater topography.

The linear dispersion relation describes the interaction between waves and bottom topography in the shallow sea and can establish a direct relationship between wavelength, wave frequency, and water depth. Research on remote sensing bathymetry based on the linear dispersion relation began in the 1990s [1,2]. It is an indirect bathymetric method that requires first acquiring wave information from remote sensing images and then calculating water depth using the linear dispersion relation. As a result, bathymetry accuracy is determined by wavelength and wave frequency. Common bathymetry approaches using optical or SAR images rely on a mass of initial water depths. However, initial water depths are difficult to obtain in some area, which limits the application of remote sensing bathymetry [3,4]. The bathymetric method used in this paper is based on the linear

dispersion relation, and it only requires a few initial water depths to acquire the entire topography covered by remote sensing images.

SAR is the main satellite for ocean wave observation, and the operational application has been mature. For example, ENVISAT ASAR, Sentinel-1, and GF-3 satellites were equipped with wave imaging modes, and many researchers had used these SAR data for ocean wave study [5–8]. The key to detecting underwater topography based on linear dispersion relation is to extract waves. Bian et al. [9] used numerical simulation to quantify the sensitivity of the bathymetry model to input parameters such as wavelength, wave period, and initial water depth. As a result, wavelength and wave period have a significant impact on bathymetry. Waves can be extracted from SAR images using common spectral analysis methods such as the fast Fourier transform, and wavelet transform. Previous researches demonstrated that FFT can stably derive wavelength and wave direction [10,11]. A series of SAR shallow sea topography detection studies had been carried out, and the SAR data used included TerraSAR-X (X-band) of Germany, ERS-2 and Sentinel-1 (C-band) of ESA, RADARSAT-2 (C-band) of Canada, ALOS-1 and ALOS-2 (L-band) of Japan, GF-3 (C-band), HJ-1C (S-band) of China, RISAT-1 (C-band) of India and COSMO-SkyMed (X-band) of Italy, etc. Most of these studies only used a single SAR image for topography detection [12–18]. The accuracy of topography detection with a single SAR image was usually low due to unfavorable sea conditions and sensor noise. In particular, the bathymetric point cannot densely cover the study area when the wave scale is large, resulting in the inability to obtain high-resolution shallow sea topography [16].

In this paper, a new approach based on multi-source SAR topography detection (MSSTD) was proposed to compensate for the shortcoming of topography detection using a single SAR image and improve detected accuracy. It can achieve dense coverage of the study area with bathymetric points and then generate high-precision topographic maps by integrating valid bathymetric depths from multi-sources SAR data. GF-3, Sentinel-1, ALOS PALSAR, and ENVISAT ASAR were used to verify the feasibility of MSSTD near Dazhou Island, Hainan Province, China, and the result revealed that this method can effectively improve the topographic detection accuracy. Section 2 introduced the linear wave theory and the fast Fourier transform (FFT). The study area, SAR data and reference depth data were described in Section 3. Section 4 is the experiment of underwater topography detection based on MSSTD. The main results were analyzed and discussed in Sections 5 and 6, and finally summarized in Section 7.

## 2. Methods

### 2.1. The Linear Wave Theory

The linear wave theory describes the propagation of ocean waves in moderately deep or shallow water. If the water depth is less than half the wavelength, the wave is in shallow water, at which point the surface wave perceives the bottom topography and is in turn shoaled and refracted. If a long sea wave propagates into shallow water, the wave is decelerated. This results in wavelength shortening. The wave height increases due to energy conservation. These two effects increase the steepness of the wave. The deceleration process coupled with the abovementioned increase in the wave height and steepness is referred to as the wave shoaling theory. If the crest of a wave is not aligned with the contour line of the bottom topography, wave refraction occurs at a certain angle between the wave direction and the contour line. For example, part of the wave near the beach propagates in shallow water and slows down more than part way from the beach.

The sea surface wave height is usually small in the shallow sea. The nonlinear process on the sea surface can be ignored, and the propagation mechanism of the sea surface wave on the surface of the uniform fluid layer can be simplified to a linear relation when the wavelength is much larger than its motion amplitude. In Equation (1), the linear dispersion

relation describes the relation between wave and water depth. In particular, it can be used to calculate water depth when the wave is in shallow water ( $d < L/2$ ) [19].

$$\omega^2 = gk \tanh(kd) \quad (1)$$

where  $\omega$  is the wave frequency ( $\omega = 2\pi/T$ ,  $T$  is wave period),  $g = 9.8 \text{ m/s}^2$  is the gravity acceleration,  $k$  is the wave number ( $k = 2\pi/L$ ,  $L$  is wavelength), and  $d$  is water depth.

The wavelength can be expressed as:

$$L = \frac{2\pi g}{\omega^2} \tanh\left(\frac{2\pi d}{L}\right) \quad (2)$$

The effect of bottom topography to wave propagation can be negligible in deep water ( $d > L/2$ ). Therefore, the wavelength in deep water is very stable. Meanwhile, the value of  $2\pi d/L$  is large, and the value of  $\tanh(2\pi d/L)$  is close to 1. Equation (2) can be simplified as [20]:

$$L = 2\pi g / \omega^2 \quad (3)$$

The wave period in the deep water can be described as:

$$T_{deep} = \sqrt{2\pi L / g} \quad (4)$$

Wave period can be considered as a stable value when waves propagate from deep water to shallow water. According to Equation (4), wavelength is the only variable of calculating wave period in deep water, so the wave period of the study area can be estimated by the wavelength in deep water [2].

Wave period can also be derived in shallow water by the linear dispersion relation, but it requires extra reference to water depth. Substituting wavelength and reference water depth into Equation (1) and wave period in shallow water can be expressed as the Equation (5):

$$T_{shallow} = \sqrt{2\pi L / \left(g \tanh\left(\frac{2\pi d_r}{L}\right)\right)} \quad (5)$$

where  $d_r$  is the reference water depth. Finally, water depth can be described as:

$$d = \frac{L}{2\pi} \operatorname{arctanh}\left(\frac{\omega^2 L}{2\pi g}\right) \quad (6)$$

## 2.2. Wave Retrieval by FFT

The wavelength and wave direction of the main wave in a certain range can be extracted by the fast Fourier transform (FFT) when the waves appear as distinct regular patterns in the SAR images. The FFT is useful for obtaining regular periodicity in images because it decomposes the function into constituent frequency components in the spatial domain. The sub-images can be converted into 2D spectrograms by FFT. The peaks in the 2D spectra indicate the wavelength and wave direction of the main waves. The wavelength and wave direction can be estimated by the following equations [21–23]:

$$L = \frac{2\pi}{\sqrt{k_x^2 + k_y^2}} \quad (7)$$

$$\varphi = \arctan\left(\frac{k_y}{k_x}\right) \quad (8)$$

where  $L$ ,  $\varphi$  are the wavelength and wave direction of the sub-image.  $k_x$ ,  $k_y$  are the peak coordinates in the wave number space, respectively. The wave direction may have a  $180^\circ$  ambiguity due to the static nature of the SAR image. In coastal areas where wave shoaling and refraction appear, the ambiguity problem can be solved after manual inspection [12].

### 3. Study Area and Data

#### 3.1. Dazhou Island

The study area in this paper is the sea area near Dazhou Island, located in the southeast Hainan Province, China, with a total area of 70 square kilometers, including a land area of 4.46 square kilometers. It is the largest island in Hainan Province. The island is abundant in plant and wildlife resources and is the unique habitat of swiftlets in China. Dazhou Island has been recognized as a national marine ecological nature reserve, which is of considerable protective value. The water depth near the island is shallow, making it difficult for ships to enter, and the traditional measurement methods may cause damage to the ecological environment. Therefore, topography detection using the remote sensing method is worthwhile for environmental protection in Dazhou Island.

The water depth is shallow around Dazhou Island and the maximum water depth does not exceed 100 m. The wave dissipation effect of the bottom topography is small. There are existing strong swells all year, which is suitable for the topography detection method based on the linear dispersion relation. Furthermore, many SAR satellites cover this region, providing ample remote sensing data. Figure 1 shows the location of Dazhou Island.

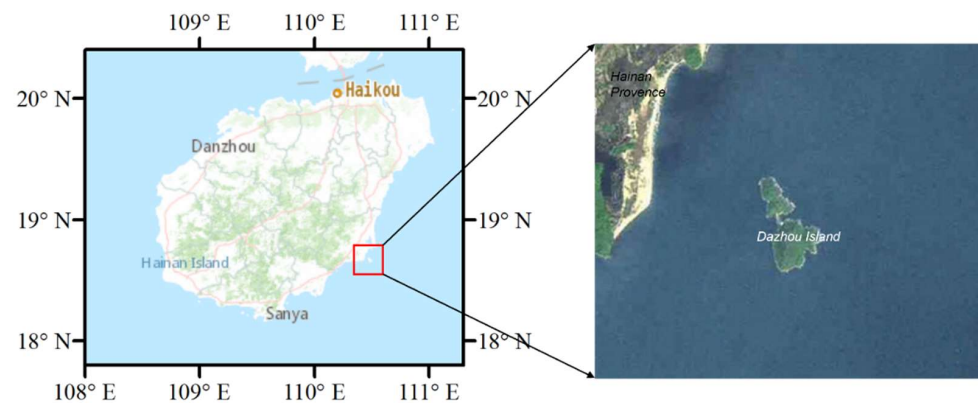


**Figure 1.** Schematic diagram of the study area, the detection area is the right figure. The left figure was produced from ArcGIS 10.2, and the right figure was produced from Google Earth.

#### 3.2. SAR Data

Four images with distinct wave patterns were chosen. Table 1 shows the details of four SAR images. The GF-3 data (18 October 2019) were generated using HH-polarized, ultra-fine strip mode (UFS) with a spatial resolution of 3 m and the level was L2. This data had been geometrically corrected, geocoded, and resampled, and no additional pre-processing was required. Sentinel-1 data was interferometric wide (IW) mode, imaged on 24 November 2018, with VV-polarized and VH-polarized. The spatial resolution was 10 m. We only used VV-polarized image for shallow sea topography detection, since the VH-polarized mode was insensitive to ocean waves. ALOS PALSAR (Fine Resolution Mode, Dual polarization (FBD), 22 September 2007) data and ENVISAT ASAR (Alternating Polarization (AP) mode, 13 March 2012) data had the same spatial resolution of 12.5 m after pre-processes. We all selected HH-polarized images. Figure 2 displays the original images and the clipped images of the study area. The wave patterns were visible in all four images.

**Table 1.** The parameters of the four satellites.

Satellite	GF-3	Sentinel-1	ALOS PALSAR	ENVISAT ASAR
Imaging Time	18 October 2019	24 November 2018	22 September 2007	13 March 2012
Band	C	C	L	C
Imaging Mode	UFS	IW	FBD	AP
Polarization	HH	VV	HH	HH
Pixel Resolution (m)	3	10	12.5	12.5

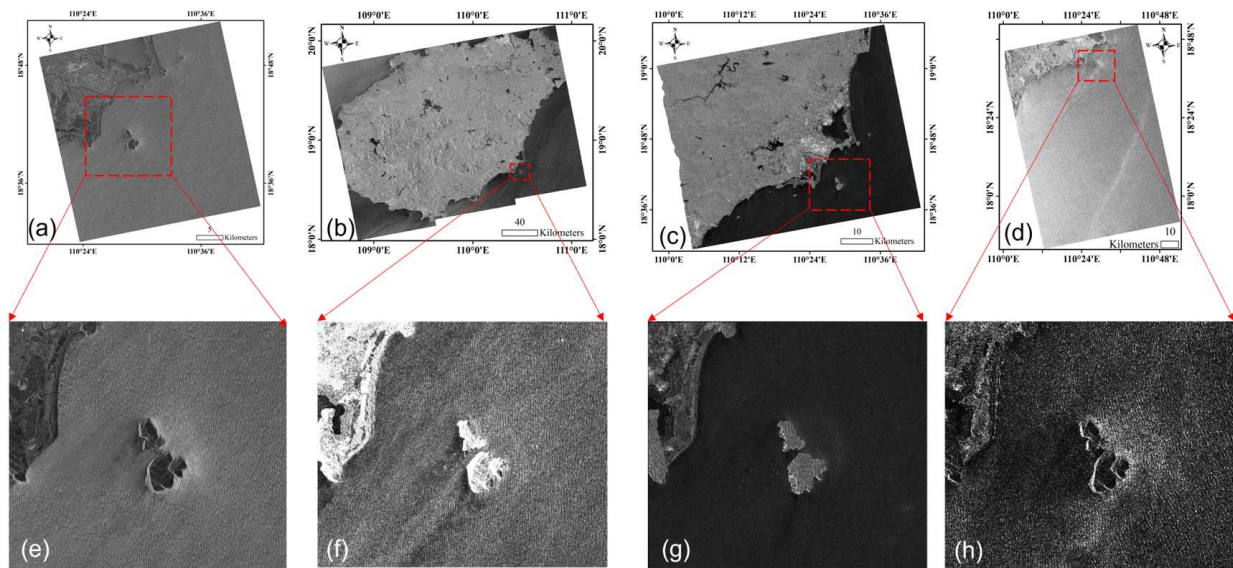


**Figure 2.** The pre-processed SAR image of the Dazhou Island: (a) GF-3 HH-polarized; (b) Sentinel-1 VV-polarized; (c) ALOS PALSAR HH-polarized; (d) ENVISAT ASAR HH-polarized. The corresponding clipped images were shown as (e–h).

### 3.3. Reference Water Depth

In this study, the reference water depth served two functions: (1) providing the initial depth for the wave period calculation; and (2) providing the comparison for the retrieved water depth from the SAR image. Global Multi-Resolution Topography (GMRT) grid data and chart data were selected as the reference water depth. GMRT synthesis is a multi-resolution compilation of edited multibeam sonar data collected by scientists and institutions worldwide, that is reviewed, processed, and gridded by the MGDS Team and merged into a single continuously updated compilation of global elevation data with the resolution of 100 m [24]. The GMRT grid data and the chart data can be download from the website [www.gmrt.org](http://www.gmrt.org) and <http://map.enclive.cn> (accessed on 8 August 2022). Figure 3 showed the water depth of chart data. We acquired a total of 561 water depth points in the study area.

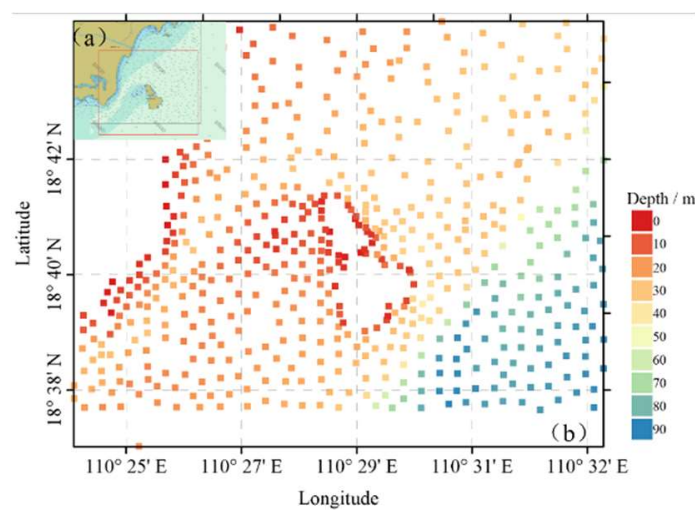


**Figure 3.** The chart data of the study area: (a) the water depths of sea area around Dazhou Island on the Chart Sever website, the selected depth points were in the red box; (b) collected water depths ranged from 0 to 90 m.

#### 4. Experiment of Underwater Topography Detection Based on MSSTD

The main steps of the experiment of underwater topography detection based on MSSTD are: (1) estimation of wave period, (2) wave retrieval, (3) calculation of water depth, (4) filtering of valid water depth and topographic synthesis. For the concise presentation, the four SAR satellites mentioned below were GF-3, Sentinel-1, ALOS PALSAR, and ENVISAT ASAR, in that order, and will not be described separately.

##### 4.1. Estimation of Wave Period

The imaging time and corresponding wave periods of the four SAR images are different. Four sub-regions far from the shore and with obvious wave patterns were chosen to estimate the wave period of each SAR image, the locations of sub-regions were noted in Figure 4. The sizes of the sub-region were set to  $512 \times 512$  pixels for GF-3 image, and  $128 \times 128$  pixels for the others SAR images. The FFT was performed on each sub-image to find the location of the peaks in the spectrum. Then the wavelength and wave direction were calculated according to Equations (7) and (8). In this paper, the reference direction was a positive-west direction, clockwise for positive directions and counterclockwise for negative directions. The wave period can be calculated by substituting the wavelength and the reference water depth into Equation (5). Then we averaged the wave periods of each sub-region as the wave period of the study area. Table 2 displays the wave parameters of various sub-regions. The result of sub-region 4 (ALOS PALSAR) was filtered out because of the unreasonable wavelength (1600 m). The final wave periods of the four images were 8.65 s, 10.13 s, 8.78 s, and 10.52 s, respectively.

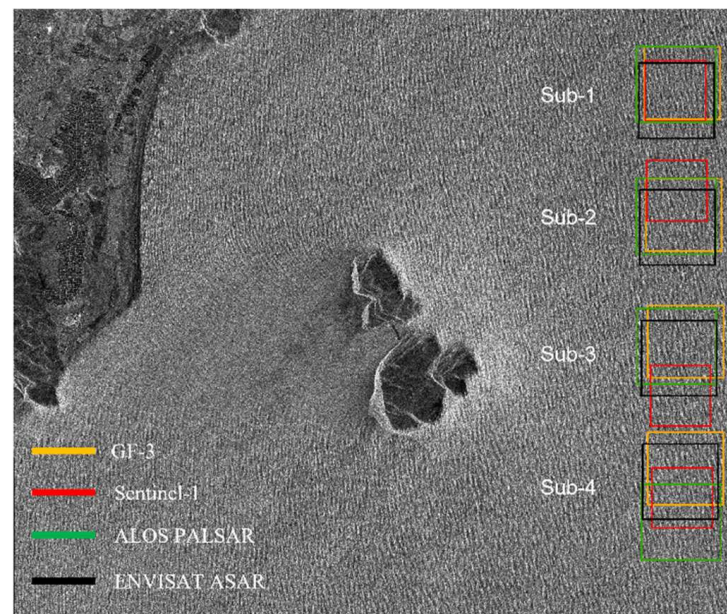


**Figure 4.** The locations of sub-regions. The yellow boxes represented the sub-region locations of GF-3, and the red, green, and black boxes represented Sentinel-1, ALOS PALSAR, and ENVISAT ASAR, respectively.

**Table 2.** The wave parameters and reference water depths of sub-regions.

Image	Sub-Region	Wavelength (m)	Wave Direction (degree)	Reference Water Depth (m)	Wave Period (s)
GF-3	1	111.24	−8.97	30.35	8.72
	2	113.77	−17.35	34.20	8.74
	3	105.49	−15.95	41.36	8.28
	4	122.30	−9.46	68.41	8.86

Table 2. Cont.

Image	Sub-Region	Wavelength (m)	Wave Direction (degree)	Reference Water Depth (m)	Wave Period (s)
Sentinel-1	1	141.35	−6.34	28.59	10.3
	2	158.76	7.13	30.96	11
	3	141.35	6.34	45.59	9.69
	4	141.35	6.34	73.39	9.53
ALOS PALSAR	1	117.63	−17.1	28.88	9.09
	2	88.75	−19.44	31.07	7.64
	3	136.70	−19.98	39.73	9.61
	4	1600	−90	75.32	-
ENVISAT ASAR	1	155.41	−29.05	28.68	11.02
	2	155.41	−29.05	31.09	10.83
	3	126.49	−18.43	41.32	9.16
	4	187.27	−20.56	68.93	11.07

#### 4.2. Wave Retrieval

Wavelength estimation is a critical step in calculating water depth using the linear dispersion relation. A small change in wavelength can result in a large change in water depth [25]. The FFT sizes of  $64 \times 64$ ,  $128 \times 128$ ,  $256 \times 256$  and  $512 \times 512$  pixels were set to estimate wave parameters and the results revealed that the bathymetry method performed best when the FFT size of GF-3 was  $256 \times 256$  pixels and the others were  $64 \times 64$  pixels.

In this paper, a grid model was adopted to retrieve waves. The wave tracking is not ideal when there are large scale wavelengths, and the grid model can retrieve the wavelengths uniformly across the entire study area [16]. The grid interval for the GF-3 image was set to 20 pixels (60 m) with a grid size of  $205 \times 232$ , and the grid interval for the Sentinel-1 image was set to 6 pixels (60 m) with a grid size of  $197 \times 236$ . The grid intervals for the ENVISAT ASAR image and the ALOS PALSAR image were set to 5 pixels (62.5 m) with a grid size of  $182 \times 209$  and  $184 \times 222$ , respectively.

In this paper, we did not consider cut-off wavelength since the waves were propagating roughly along the SAR range direction in the four SAR images. According to the nature of linear dispersion relation, one wave period corresponds to one wavelength maximum, i.e.,  $L_{max} = \frac{gT^2}{2\pi}$ . The  $L_{max}$  corresponding to the four SAR images were 116.43 m, 160.05 m, 120.24 m, and 172.61 m in order, which can constrain the wavelength calculation and avoid large-scale waves. Gridded wavelength estimation was performed on four images, and then the original estimation results were filtered using  $L_{max}$  to obtain wavelengths that can be used for bathymetry. The wavelength results were shown in Figure 5. The estimation result of GF-3 was significantly better than the other three images, with few blank areas except for land. The blank area mainly existed west of Dazhou Island, and it was explained in Figure 2e that the wave patterns in this area were invisible. This phenomenon occurred in all four images. The waves were refracted or diffracted when propagating to the island, causing inconspicuous waves in the west area of Dazhou Island. The Sentinel-1 wavelength result showed some large blank areas around Dazhou Island, particularly in the southwest. We can discover that there were also some large-scale streaks (see Figure 2f), which led to a large error in the wavelength calculation. In addition, the wavelength results of ALOS PALSAR and ENVISAT ASAR images were worse than the GF-3 image and Sentinel-1. It was not difficult to notice that the wave patterns of ALOS PALSAR and ENVISAT ASAR were not as distinct as those of GF-3 and Sentinel-1 in Figure 2.

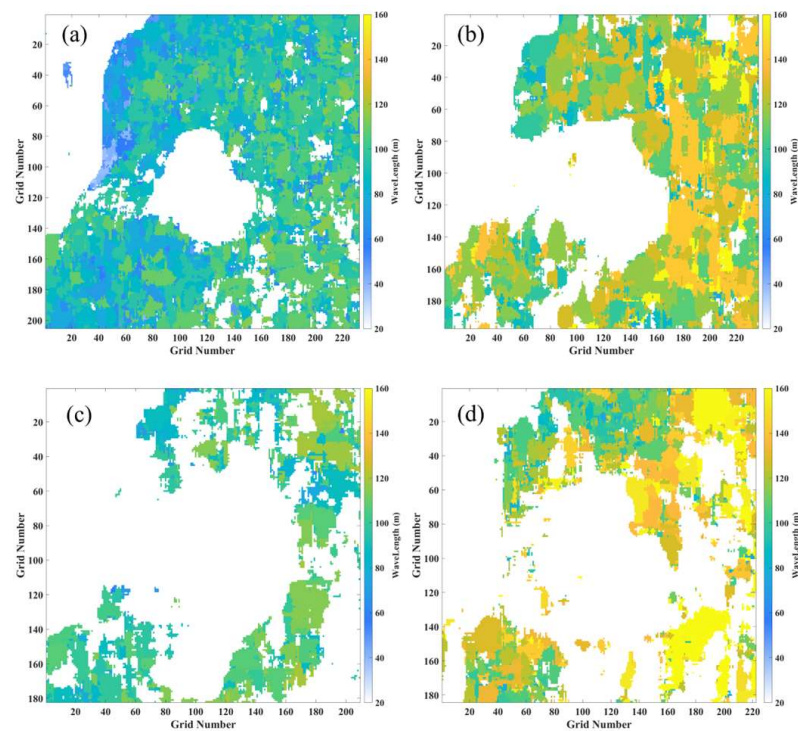


**Figure 5.** The wavelength results. The blank areas are land or wavelengths greater than the wavelength maximum. (a) GF-3, (b) Sentinel-1, (c) ALOS PALSAR, (d) ENVISAT ASAR.

#### 4.3. Calculation of Water Depth

The water depth can be deduced from the linear dispersion relation by substituting wavelength and wave period into Equation (6) when the shallow water condition is satisfied. The bathymetry results were displayed in the Figure 6. The water depth mainly ranged from 10 to 30 m.

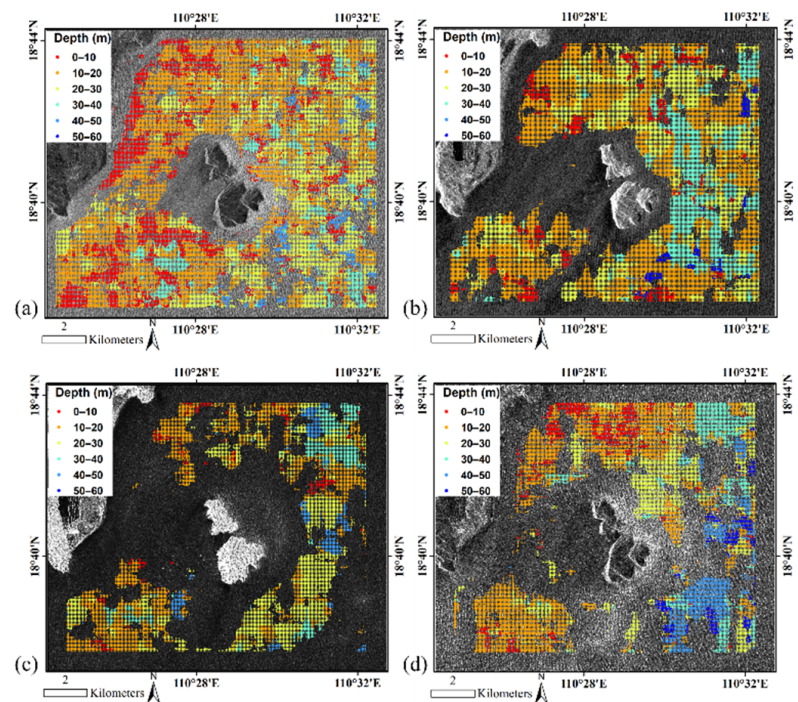


**Figure 6.** Bathymetry results. GF-3, Sentinel-1, ALOS PALSAR, and ENVISAT ASAR were shown in the (a–d).

The water depth values deduced from different SAR images varied even for the same location. Not every bathymetric value was accurate, so a preliminary error assessment of the bathymetric values was necessary. We adopted GMRT grid data to make the preliminary error assessment. Three indexes were used to evaluate the error of bathymetry, these were:

- (1) Mean Absolute Error (MAE)

$$\text{MAE} = \frac{\sum_{i=1}^n |d_i - r_i|}{n} \quad (9)$$

- (2) Mean Relative Error (MRE)

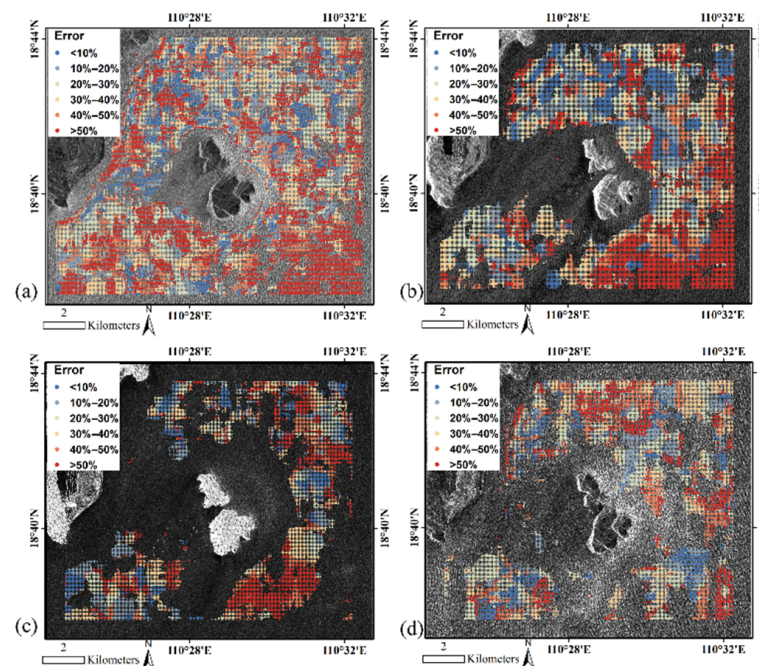
$$\text{MRE} = \frac{\sum_{i=1}^n \left| \frac{d_i - r_i}{d_i} \right|}{n} \quad (10)$$

- (3) Correlation Coefficient (R)

$$R = \frac{\sum_{i=1}^n (d_i - \bar{d})(r_i - \bar{r})}{\sqrt{\sum_{i=1}^n (d_i - \bar{d})^2} \sqrt{\sum_{i=1}^n (r_i - \bar{r})^2}} \quad (11)$$

where  $d_i$  and  $r_i$  are the detected and reference depths,  $\bar{d}$  and  $\bar{r}$  are the average values of detected and reference depths, respectively.

Table 3 presented the bathymetry error of four SAR images. The MAEs of four SAR images were 12.27, 13.19, 11.62, and 9.92 m, with the MREs of 39.54%, 36.27%, 36.11%, and 33.33%, respectively. The error was divided into six parts: less than 10%, 10–20%, 20–30%, 30–40%, 40–50% and greater than 50% (Figure 7). The blue dots indicated that the MRE was less than 10%, and the red dots indicated that the MRE was greater than 50%. The points with high bathymetric error were mainly located in the southeastern region of Dazhou Island. In previous studies [26,27], the water depths were less than 50 m, while Figure 3 showed that the actual water depths in this area were greater than 70 m, posing a challenge to the bathymetry based on linear wave theory.

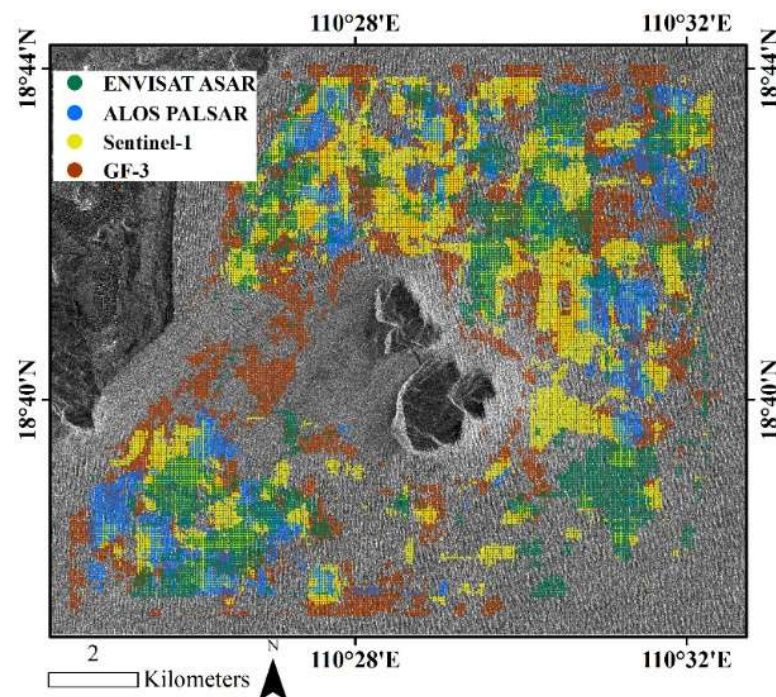


**Figure 7.** Error of retrieval depths, GF-3, Sentinel-1, ALOS PALSAR, and ENVISAT ASAR were shown in the (a–d). The blue dots indicated that the MRE was less than 10%, and the red dots indicated that the MRE was greater than 50%.

**Table 3.** The bathymetry error of different images.

Image	MAE (m)	MRE	Number
GF-3	12.27	39.54%	32,788
Sentinel-1	13.19	36.27%	26,422
ALOS PALSAR	11.62	36.11%	11,471
ENVISAT ASAR	9.92	33.33%	16,466

The retrieved water depth with MRE less than 20% was defined as the valid depth. Figure 8 shows the synthesis of valid depths based on multi-source SAR data. Compared with the result of a single SAR image, the bathymetry coverage of multi-source SAR is significantly improved.

**Figure 8.** Integrated schematic of valid water depth, the green, blue, yellow, brown dots present the locations of valid water depth from ENVISAT ASAR, ALOS PALSAR, Sentinel-1, GF-3 images, respectively.

#### 4.4. Filtering of Valid Water Depth

The detection accuracy will be low if the topography is interpolated using only the bathymetry values from a single SAR image. The location distribution of valid depth points varied greatly. The large coverage of the study area could be realized by combining the valid depths from different SAR images.

Table 4 presented the error of valid depth. The MAEs were 3.30, 2.92, 2.40, and 3.37 m of the four SAR images with the MREs of 13.78%, 11.41%, 10.94%, and 12.40%, respectively. The number of valid depths was not considered in this section, so the MAE or MRE cannot be used as the sole indicator to evaluate the quality of bathymetry.

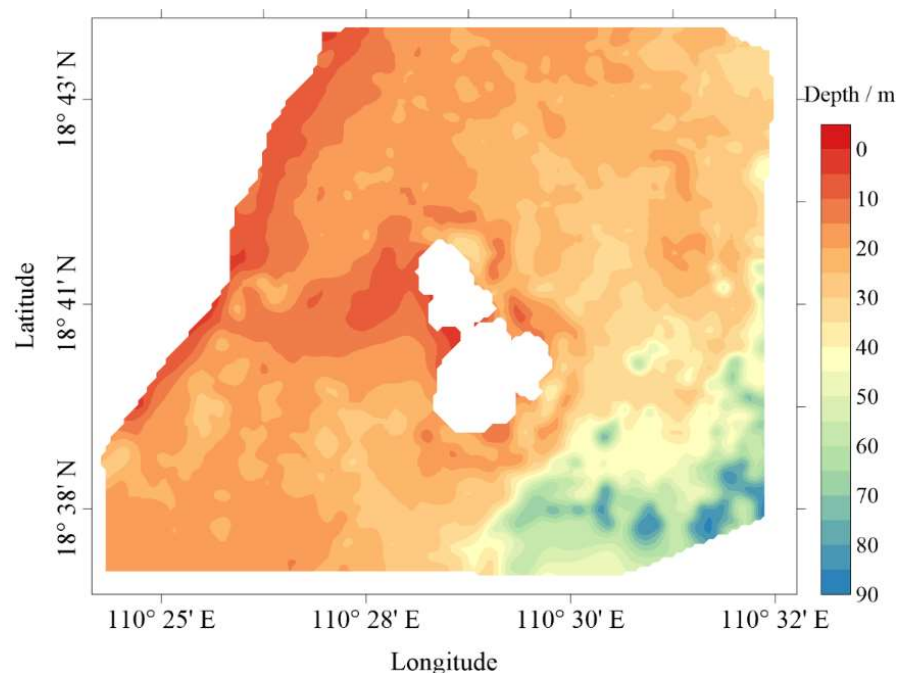
**Table 4.** Errors of valid depths.

Image	MAE (m)	MRE	Number
GF-3	3.30	13.78%	10,168
Sentinel-1	2.92	11.41%	8738
ALOS PALSAR	2.40	10.94%	3837
ENVISAT ASAR	3.37	12.40%	7549

## 5. Results

### 5.1. Topography from MSSTD

There were few valid depths in the west and southeast of Dazhou Island, so the chart data was adopted to fill in for this lack of information. Finally, all the valid depths were subjected to kriging interpolation and two-dimensional low pass filtering to generate underwater topography (see in the Figure 9). The study area has a minimum water depth of about 0 m and a maximum water depth of about 90 m. The depth gradually decreases roughly along the southeast-to-northwest axis. The waters of the near-shore and the west side of Dazhou Island are shallow, ranging from 0 to 20 m, and the topography changes slowly. The underwater topographic gradient in the southeast waters of Dazhou Island is large, with depths increasing rapidly from 20 to 90 m. The variation tendency of the detected topography and the chart data (see Figure 3) are highly consistent.



**Figure 9.** The topography retrieved from MSSTD. It was produced by interpolation of the valid water depths. The upper left and center blank areas were land and Dazhou Island, respectively.

### 5.2. Comparison between Detected Topography and the Chart Depth

Chart depth data was adopted to evaluate the topography result between MSSTD and different satellites. We only discussed the area with a depth of 0–50 m, since the error in the southeast (deeper than 50 m) of Dazhou Island was too large (see in Figure 7). Figure 10 shows the scatter plots of retrieved topography and chart data, where MSSTD performs better than other satellite with the MAE of 2.90 m, MRE of 14.13%, and correlation coefficient (R) of 0.92. Wiehle et al. [28] used high-resolution TerraSAR-X images to detect the topography of the Jersey Island Sea and obtained errors of 6.5, 6.7, and 7.7 m at 10–20, 20–30, and 30–40 m, respectively (compared with GEBCO data). Roeber et al. [14] obtained water depths of 5–25 m with an error of 2.65 m (compared with measured water depth). The water depth of the study area is 0–50 m and the error compared to the chart data is 2.9 m. The detection accuracy is significantly better than previous studies, proving that MSSTD can effectively derive shallow sea topography (0–50 m) with high accuracy. The topography detection errors of GF-3, Sentinel-1, and ENVISAT ASAR are nearly identical, but they are all significantly better than ALOS PALSAR.

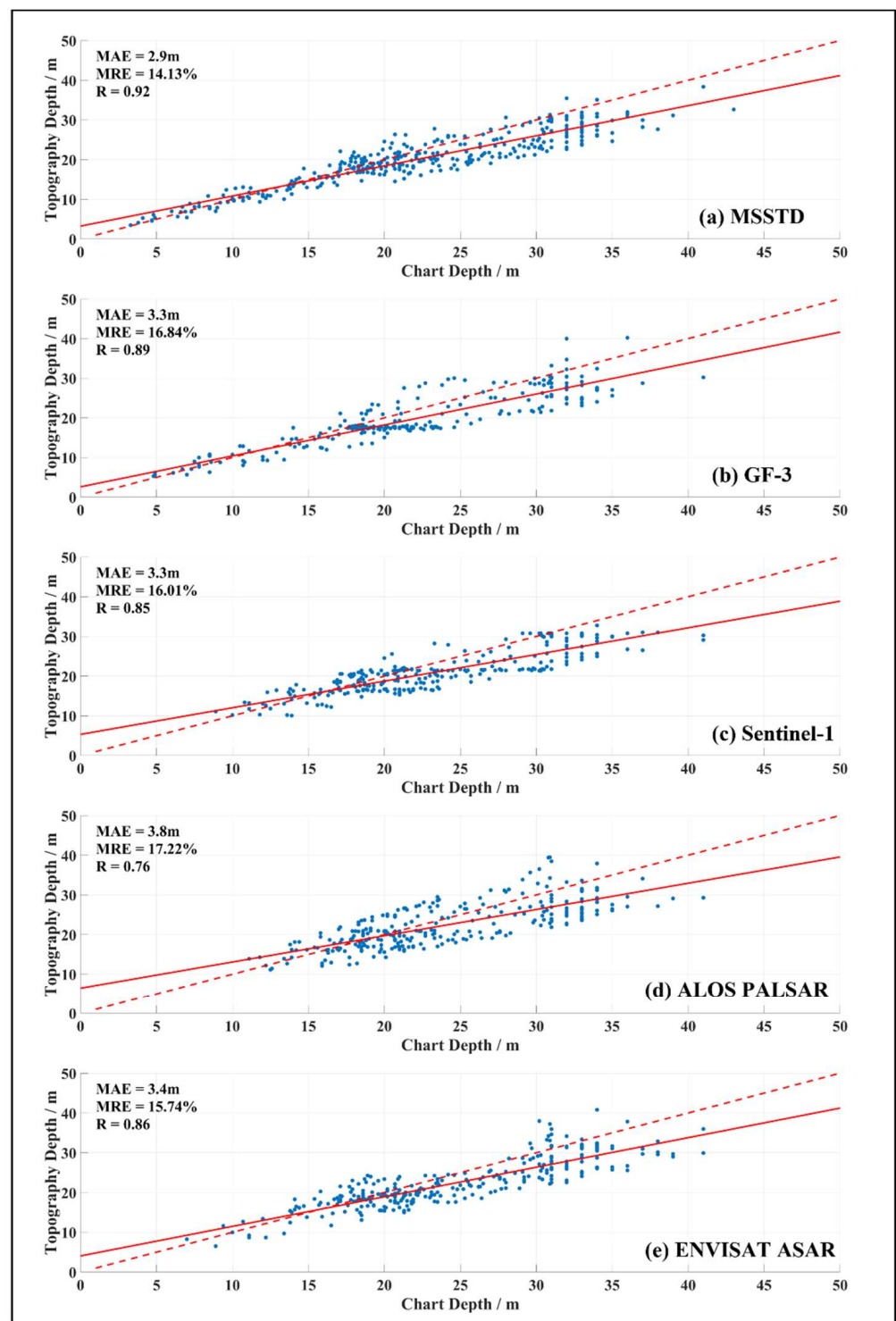


**Figure 10.** Scatter plots of retrieved topography and chart data. The red dash line is the 1:1 line and red solid line is the linear fit line. The index R is the linear correlation coefficient.

## 6. Discussions

### 6.1. Influence of Satellite Parameters on Bathymetry

This section analyzed the ability of four different SAR to detect underwater topography. According to Section 3.2, the grid point numbers of four SAR images were 47,560, 46,492, 38,038, and 40,848, respectively. The bathymetry point numbers were 32,788, 26,422, 11,471, and 16,466, respectively, after eliminating the points on the land or with abnormal wavelengths. The number of detected water depth points can be equated to the number of

effective wavelength points under certain wave period conditions. Clear and regular wave patterns in the SAR image facilitate wavelength extraction. GF-3 had the highest resolution of 3 m, so it detected the largest number of bathymetry points. Sentinel-1 had a higher resolution of 10 m than ALOS PALSAR and ENVISAT ASAR (12.5 m), correspondingly to more bathymetry points. Based on the result in this study, high spatial resolution can enhance the ability of wave extraction and the accuracy of bathymetry. For a specific wavelength, the wave extraction ability may not continue to increase when the image spatial resolution reaches a certain level.

In the perspective of detection error, ENVISAT ASAR had the highest bathymetry accuracy, followed by ALOS PALSAR, Sentinel-1, and GF-3. The MAE and MRE in Table 3 cannot fully represent the detection accuracy of SAR images. Although the detection error of GF-3 was the largest among the four SAR images, it also had the largest number of bathymetry points, almost three times that of ALOS PALSAR. GF-3 had the best detection ability after the comprehensive comparison. Figure 2g shows that the wave patterns on the ALOS PALSAR image are not noticeable compared to other images, which contributes to the lower number of valid depth points.

The SAR image of Sentinel-1 is VV-polarized, and the others are HH-polarized. In this study, polarization (between HH and VV) did not notably influence the topography detection. For the detection accuracy, there was little difference between the HH and VV-polarized of one view SAR image, with the difference smaller than 10% in the Bian et al. [15] study and the difference smaller than 5% in the Huang et al. [16] study. Higher radar frequency produces stronger backscatter intensity of the sea surface. However, smaller radar frequencies produce more distinct contrast on the SAR image, which can contribute to wave extraction [29]. The band of GF-3 (5.4 GHz), Sentinel-1 (5.4 GHz), and ENVISAT ASAR (5.3 GHz) is C band, and ALOS PALSAR (1.27 GHz) is L band. There were not distinct bright and dark stripes on the ALOS PALSAR image (see Figure 2g), which may be due to the absence of strong swells.

In summary, sensor band and polarization (HH-polarized and VV-polarized) have little effect on shallow sea bathymetry in this study. In contrast, spatial resolution markedly impacts the accuracy of bathymetry, and high resolution can improve wave extraction and thus the accuracy of topography detection.

## 6.2. Influence of FFT on Bathymetry

MREs of bathymetry when the size of FFT was set to  $32 \times 32$ ,  $64 \times 64$ ,  $128 \times 128$ ,  $256 \times 256$ , and  $512 \times 512$  pixels were shown in the Figure 11. The pixel numbers of Sentinel-1, ALOS PALSAR and ENVISAT ASAR images are  $1316 \times 1555$ ,  $1046 \times 1184$  and  $1056 \times 1246$ , respectively. Many detected points on the image edge would be missed when the size of FFT was set to  $512 \times 512$  pixels. Therefore, the maximum size of the FFT for these three images was set to  $256 \times 256$  pixels. GF-3 image performed best when the size of the FFT was set to  $256 \times 256$  pixels with the MRE of 13.87%. Sentinel-1, ALOS PALSAR, and ENVISAT ASAR images had the smallest error when the size of the FFT was set to  $64 \times 64$  pixels with the MREs of 11.41%, 10.94%, and 12.40%, respectively. The size of the FFT is crucial for wave extraction because the wavelength retrieved by FFT is the dominant wavelength. The FFT size of the four SAR images was converted to length units of  $768 \text{ m} \times 768 \text{ m}$ ,  $640 \text{ m} \times 640 \text{ m}$ ,  $800 \text{ m} \times 800 \text{ m}$ , and  $800 \text{ m} \times 800 \text{ m}$ , respectively. The main ranges of retrieved wavelengths for the four images are 80–110 m, 100–130 m, 90–120 m, and 120–160 m, as shown in Figure 5. We discovered that the bathymetry error was minimized when 5–10 waves were included in the FFT frame. This is consistent with the research of Shen et al. [30].

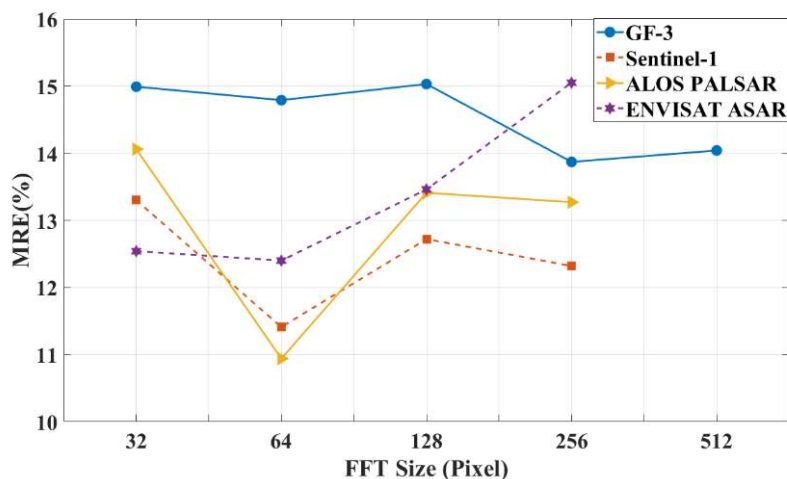


Figure 11. Line chart of bathymetry error of different FFT sizes.

6.3. Sensitivity Analysis of MSSTD to Different Water Depth

In this section, we discussed the sensitivity of MSSTD to the water depth, and the errors of the four SAR images from a different range of water depths were shown in Figure 12. GF-3, Sentinel-1 and ALOS PALSAR images all had a minimum detection error in the water depths of 10–20 m (only 7 water depth points in 50–60 m of Sentinel-1 image, the sample was too small to analyze). ENVISAT ASAR image performed best in the water depths of 40–50 m, followed by 10–20 m. In conclusion, MSSTD has the best performance in the water depths of 10–20 m.

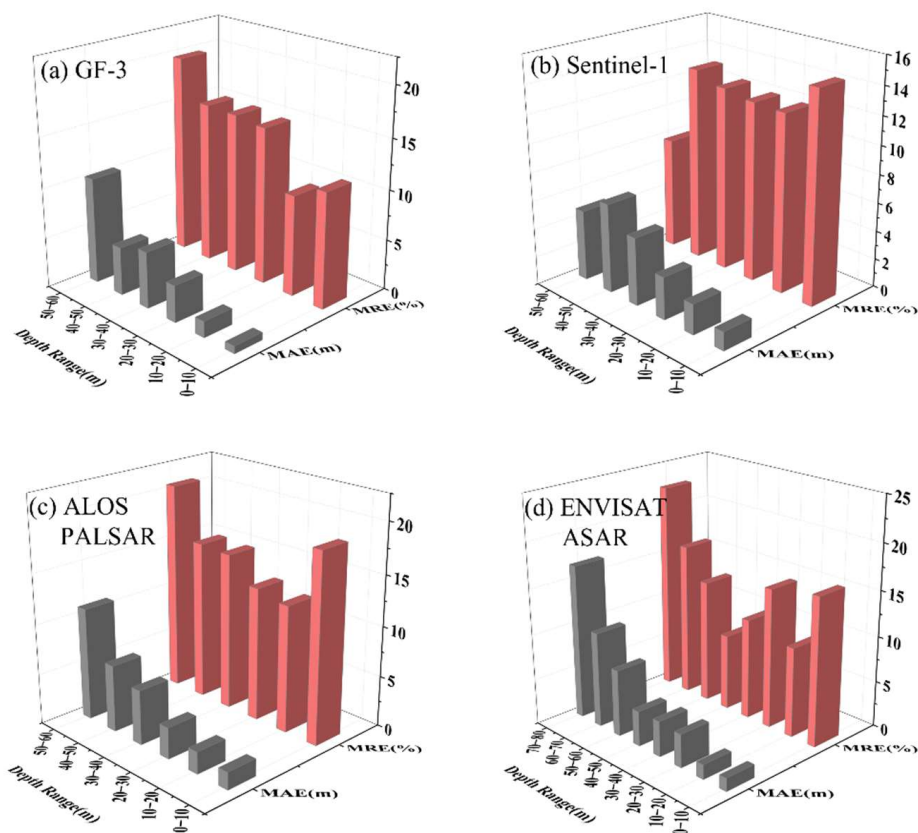


Figure 12. Error distribution in different water depth ranges. The black bar is the MAE and red bar is the MRE.

The MREs of four images were larger in the water depths of 0–10 m. Figure 9 revealed that the areas with a 0–10 m depth were mainly located in the nearshore and west area of Dazhou Island. (1) Wave breaking, coastal and offshore currents exist nearshore, (2) tide correction was not applied to the bathymetry results, and 0–10 m was greatly influenced by tides, and (3) commonly the area to the west of Dazhou island is shadowed and cannot be used in bathymetry retrieval. The above all contributed to the large error of MSSTD in the water depth of 0–10 m. Some water depths (exceeding 50 m) and corresponding wavelengths retrieved from SAR images (Figure 5) did not satisfy the shallow sea relation ( $d < L/2$ ), which may result in the unsatisfactory bathymetry error when the water depth exceeded 50 m.

Note that the water depths between 20–50 m are consistently underestimated for all four individual satellites and MSSTD in Figure 10. Based on the nature of the linear dispersion relation (Equation (1)), both overestimation of wave period and underestimation of wavelength could result in underestimation of water depth. The depths of the whole range instead of only 20–50 m should be underestimated if the wave period is overestimated. It's more likely to be the underestimation of wavelength or interpolation method that produces the phenomenon.

#### 6.4. Limitation of MSSTD

MSSTD proposed in this paper is based on linear wave theory that can well describe the interaction between waves and bottom topography in shallow seas (water depth less than half of the wavelength). However, this method has some limitations and is “particular” about the study area and SAR data. First, MSSTD is an indirect bathymetry, which requires bathymetry from waves, so there must be visible wave patterns in SAR images. Accurate wavelength and wave period are the prerequisites for bathymetry. Secondly, MSSTD is only applicable to shallow seas. The interaction between waves and bottom topography is weak in the deep sea, thus causing unsatisfactory bathymetry error. Wave imaging can be assumed to be linear in this paper because the waves on the four SAR images propagate approximately along the SAR range direction. SAR wave imaging is a complex process with nonlinear velocity clustering effects in the azimuth direction [22]. Particularly, SAR cannot image waves with wavelengths smaller than cut-off wavelengths in the azimuth direction due to satellite parameters and sea state. The cut-off wavelength should be considered for waves propagating along the SAR azimuth direction.

## 7. Conclusions

In this work, a new shallow sea topography detection model based on multi-source SAR (MSSTD) was proposed to improve the accuracy of topography detection. The underwater topography around Dazhou Island, Hainan, Province, China was detected using GF-3, Sentinel-1, ALOS PALSAR, and ENVISAT ASAR data. Compared with the chart data, the errors of MSSTD were all better than that of a single SAR image, with a MAE of 2.9 m, MRE of 14.13%, and R of 0.92, respectively. MSSTD can utilize the advantages of different SAR images to jointly generate a high-precision underwater topography. The detected results shows the water depth of the study area varies from 0–90 m. In the southeast of Dazhou Island, the water depth and topographic gradient are deeper and larger, while they are shallower and smaller in other areas. GF-3 had the best bathymetry among the four SAR images, and although the MAR and MRE of GF-3 were not the minimum, the valid depth points of GF-3 were far more than the other three SAR images. In contrast to polarization and radar band, image resolution had a significant impact on bathymetry. Moreover, we also analyzed the effect of FFT on bathymetry, and the results showed that MSSTD performed better when the size of FFT was 5–10 times the wavelength. The sensitivity to various ranges of water depth was discussed in this paper to investigate the performance of MSSTD. The model performed best in water depths of 10–20 m, while it struggled with too shallow (0–10 m) or deeper water depths (>50 m). Although MSSTD is particular about the

study area and SAR data, it still shows the potential to derive high-precision underwater topography in some specific areas.

Many countries have launched a series of SAR satellites, providing a mass of data for ocean research. In the future, more SAR data can be used to study new algorithms to improve the accuracy of shallow sea topography detection.

**Author Contributions:** L.H. developed the methodology, performed the experiments and analysis, and wrote the manuscript; J.Y., J.M. and C.F. provided the conceptualization and revised the manuscript; J.Z. revised the manuscript. All authors have read and agreed to the published version of the manuscript.

**Funding:** This research was funded by the Innovation Group Project of Southern Marine Science and Engineering Guangdong Laboratory (Zhuhai) (311021004), the National Natural Science Foundation of China, grant number 51839002, the National Natural Science Foundation of China, grant number U2006207, and the Project of State Key Laboratory of Satellite Ocean Environment Dynamics, Second Institute of Oceanography, Ministry of Natural Resources (SOEDZZ2205).

**Data Availability Statement:** Not applicable.

**Acknowledgments:** We gratefully acknowledge the National Satellite Ocean Application Service (NSOAS) for providing the GF-3 SAR productions, ASF for Sentinel-1 and ALOS PALSAR data, and ESA for ENVISAT ASAR data. Furthermore, we gratefully acknowledge OpenTopography and ChartServer for providing GMRT data and the chart depth of study area.

**Conflicts of Interest:** The authors declare no conflict of interest.

## References

- Bell, P.S. Shallow Water Bathymetry Derived from an Analysis of X-Band Marine Radar Images of Waves. *Coast. Eng.* **1999**, *37*, 513–527. [[CrossRef](#)]
- Leu, L.-G.; Kuo, Y.-Y.; Liu, C.-T. Coastal bathymetry from the wave spectrum of spot images. *Coast. Eng. J.* **1999**, *41*, 21–41. [[CrossRef](#)]
- Cao, B.; Deng, R.; Zhu, S.; Liu, Y.; Liang, Y.; Xiong, L. Bathymetric Retrieval Selectively Using Multiangular High-Spatial-Resolution Satellite Imagery. *IEEE J. Sel. Top. Appl. Earth Obs. Remote Sens.* **2021**, *14*, 1060–1074. [[CrossRef](#)]
- Huang, L.; Yang, J.; Meng, J.; Zhang, J. Underwater Topography Detection and Analysis of the Qilianyu Islands in the South China Sea Based on GF-3 SAR Images. *Remote Sens.* **2020**, *13*, 76. [[CrossRef](#)]
- Fan, C.; Wang, X.; Zhang, X.; Gao, D. A Newly Developed Ocean Significant Wave Height Retrieval Method from Envisat ASAR Wave Mode Imagery. *Acta Oceanol. Sin.* **2019**, *38*, 120–127. [[CrossRef](#)]
- Li, H.; Stopa, J.E.; Mouche, A.; Zhang, B.; He, Y.; Chapron, B. Assessment of Ocean Wave Spectrum Using Global Envisat/ASAR Data and Hindcast Simulation. *Remote Sens. Environ.* **2021**, *264*, 112614. [[CrossRef](#)]
- Wang, H.; Yang, J.; Lin, M.; Li, W.; Zhu, J.; Ren, L.; Cui, L. Quad-Polarimetric SAR Sea State Retrieval Algorithm from Chinese Gaofen-3 Wave Mode Images via Deep Learning. *Remote Sens. Environ.* **2022**, *273*, 112969. [[CrossRef](#)]
- Wang, H.; Wang, J.; Yang, J.; Ren, L.; Zhu, J.; Yuan, X.; Xie, C. Empirical Algorithm for Significant Wave Height Retrieval from Wave Mode Data Provided by the Chinese Satellite Gaofen-3. *Remote Sens.* **2018**, *10*, 363. [[CrossRef](#)]
- Bian, X.; Shao, Y.; Zhang, C.; Xie, C.; Tian, W. The Feasibility of Assessing Swell-Based Bathymetry Using SAR Imagery from Orbiting Satellites. *ISPRS J. Photogramm. Remote Sens.* **2020**, *168*, 124–130. [[CrossRef](#)]
- Pereira, P.; Baptista, P.; Cunha, T.; Silva, P.A.; Romão, S.; Lafon, V. Estimation of the Nearshore Bathymetry from High Temporal Resolution Sentinel-1A C-Band SAR Data—A Case Study. *Remote Sens. Environ.* **2019**, *223*, 166–178. [[CrossRef](#)]
- Santos, D.; Abreu, T.; Silva, P.A.; Baptista, P. Estimation of Coastal Bathymetry Using Wavelets. *JMSE* **2020**, *8*, 772. [[CrossRef](#)]
- Brusch, S.; Held, P.; Lehner, S.; Rosenthal, W.; Pleskachevsky, A. Underwater Bottom Topography in Coastal Areas from TerraSAR-X Data. *Int. J. Remote Sens.* **2011**, *32*, 4527–4543. [[CrossRef](#)]
- Fan, K.; Huang, W.; He, M.; Fu, B.; Zhang, B.; Chen, X. Depth Inversion in Coastal Water Based on SAR Image of Waves. *Chin. J. Ocean. Limnol.* **2008**, *26*, 434–439. [[CrossRef](#)]
- Roerber, V.; Ranchin, T.; Dubranna, J.; Cloarec, M. Extraction of Bathymetric Features Using Multiple SAR Images Produced by Sentinel-1. In *Proceedings of the Sixth International Conference on Remote Sensing and Geoinformation of the Environment (RSCy2018)*; Themistocleous, K., Hadjimitsis, D.G., Michaelides, S., Ambrosia, V., Papadavid, G., Eds.; SPIE: Paphos, Cyprus, 2018; p. 22.
- Bian, X.; Shao, Y.; Tian, W.; Wang, S.; Zhang, C.; Wang, X.; Zhang, Z. Underwater Topography Detection in Coastal Areas Using Fully Polarimetric SAR Data. *Remote Sens.* **2017**, *9*, 560. [[CrossRef](#)]
- Huang, L.; Fan, C.; Meng, J.; Yang, J.; Zhang, J. Shallow Sea Topography Detection Using Fully Polarimetric Gaofen-3 SAR Data Based on Swell Patterns. *Acta Oceanol. Sin.* **2022**, *41*, 13.

17. Bian, X.; Shao, Y.; Tian, W.; Zhang, C. Estimation of Shallow Water Depth Using HJ-1C S-Band SAR Data. *J. Navig.* **2016**, *69*, 113–126. [[CrossRef](#)]
18. Mishra, M.K.; Ganguly, D.; Chauhan, P. Ajai Estimation of Coastal Bathymetry Using RISAT-1 C-Band Microwave SAR Data. *IEEE Geosci. Remote Sens. Lett.* **2014**, *11*, 671–675. [[CrossRef](#)]
19. LeBlond, P.H.; Mysak, L.A. *Waves in the Ocean*; Elsevier: Amsterdam, The Netherlands, 1981.
20. Howd, P. *Beach Processes and Sedimentation*; Wiley: Hoboken, NJ, USA, 1998.
21. Bruck, M.; Lehner, S. Coastal Wave Field Extraction Using TerraSAR-X Data. *J. Appl. Remote Sens.* **2013**, *7*, 073694. [[CrossRef](#)]
22. Collard, F.; Ardhuin, F.; Chapron, B. Extraction of Coastal Ocean Wave Fields From SAR Images. *IEEE J. Ocean. Eng.* **2005**, *30*, 526–533. [[CrossRef](#)]
23. Li, X.; Lehner, S.; Rosenthal, W. Investigation of Ocean Surface Wave Refraction Using TerraSAR-X Data. *IEEE Trans. Geosci. Remote Sens.* **2010**, *48*, 830–840. [[CrossRef](#)]
24. Arko, R.; Ryan, W.; Carbotte, S.; Melkonian, A.; Coplan, J.; O'Hara, S.; Chayes, D.; Weissel, R.; Goodwillie, A.; Ferrini, V.; et al. The Global Multi-Resolution Topography (GMRT) Synthesis. In Proceedings of the AGU Fall Meeting Abstracts, San Francisco, CA, USA, 10–14 December 2007; Volume 2007, p. IN51B-0405.
25. Boccia, V.; Renga, A.; Rufino, G.; D'Errico, M.; Moccia, A.; Aragno, C.; Zoffoli, S. Linear Dispersion Relation and Depth Sensitivity to Swell Parameters: Application to Synthetic Aperture Radar Imaging and Bathymetry. *Sci. World J.* **2015**, *2015*, 374579. [[CrossRef](#)] [[PubMed](#)]
26. Misra, A.; Ramakrishnan, B.; Muslim, A.M. Synergistic Utilization of Optical and Microwave Satellite Data for Coastal Bathymetry Estimation. *Geocarto Int.* **2022**, *37*, 2323–2345. [[CrossRef](#)]
27. Wiehle, S.; Pleskachevsky, A. Bathymetry Derived from Sentinel-1 Synthetic Aperture Radar Data. In Proceedings of the EUSAR 2018, 12th European Conference on Synthetic Aperture Radar, Aachen, Germany, 4–7 June 2018; VDE: Frankfurt am Main, Germany, 2018; pp. 1–4.
28. Wiehle, S.; Pleskachevsky, A.; Gebhardt, C. Automatic Bathymetry Retrieval from SAR Images. *CEAS Space J.* **2019**, *11*, 105–114. [[CrossRef](#)]
29. Jackson, C.R.; Apel, J.R. *Synthetic Aperture Radar: Marine User's Manual*; U.S. DEPARTMENT OF COMMERCE National Oceanic and Atmospheric Administration: Washington, DC, USA, 2004.
30. Shen, S.; Zhu, S.; Kang, Y.; Zhang, W.; Cao, G. Simulation analysis for remote sensing inversion of wavelength and water depth by the Fast Fourier Transform method. *J. East China Norm. Univ. (Nat. Sci.)* **2019**, *2*, 148.